Impact of Particle Morphology on Surface Oxidation of Nanoparticles: A Kinetic Monte Carlo Based Study

Dibyendu Mukherjee
Sustainable Energy Education and Research Center (SEERC), Dept. of Mechanical, Aerospace and Biomedical Engineering, University of Tennessee, Knoxville, TN 37996

Matthew Wang and Bamin Khomami
Sustainable Energy Education and Research Center (SEERC), Material Research and Innovation Laboratory (MRAIL), Dept. of Chemical and Biomolecular Engineering, University of Tennessee, Knoxville, TN 37996

DOI 10.1002/aic.13740
Published online March 12, 2012 in Wiley Online Library (wileyonlinelibrary.com).

A high-fidelity coagulation driven kinetic Monte Carlo (KMC) model is developed to study the physics of the nonlinear interplay between competing exothermic collision-coalescence mediated surface oxidation and complex morphologies in aggregated nanostructures generated during gas-phase synthesis of nanoparticles. Results suggest a twofold oxidation mechanism in which thermally activated processes form a critical oxide shell, beyond which morphological complexity of nanoparticles gives rise to enhanced oxidation. Simulation results for the example case-study of Al nanoparticle synthesis in air under different prototypical processing conditions, i.e., temperature, pressure and volume loading, show the efficacy of the model in determining optimal process variables for tuning the structural and chemical makeup of energetic nanomaterials. Finally, it is demonstrated that inclusion of nonisothermal coalescence that leads to the formation of fractal-like nanoparticles (particularly, < 15 nm) gives rise to higher degrees of oxidation when compared to instantly coalescing spherical particles. © 2012 American Institute of Chemical Engineers *AIChE J,* 58: 3341–3353, 2012
Keywords: surface fractal dimension, metal nanoparticles, particle morphology, KMC model, oxidation

Introduction

Nanoparticle manufacturing via flame synthesis,[1,2] plasma processing,[3] or flow reactors[4,5] has been extensively used for the fabrication of nanostructured materials and thin films with controlled porosity, specific surface coatings and catalytic properties. These applications either require compact spherical nanoparticles with low-surface area (electronic device fabrications, sensors, etc.), or fractal-like aggregates with high-surface area (nanocatalysts, energetic materials, H_2 storage, etc.). Yet, the complex interplay between various chemical/physical pathways such as collision, coalescence and surface reactivity during gas-phase synthesis of these structures is not clearly understood.

Although aerosol dynamics based sectional/nodal models,[6–8] method of moments[9,10] or models for particle laden flows[11,12] have been widely used to study nanoparticle evolution in the past, only recent Monte Carlo (MC) based stochastic models are able to simulate nanoparticle nucleation, coagulation, aggregation, surface growth and restructuring[13,14] without resorting to a single unifying governing multivariate equation.[15] Specifically, MC simulations of nanoparticle aggregation and restructuring via coalescence/sintering[16] have provided great insight into the role of process parameters in controlling the structures of gas-phase synthesized nanoparticles.[17] Furthermore, the highly exothermic and energetic nature of coalescence due to self-reinforcing atomic diffusions at nanoscale[18,19] have prompted recent kinetic MC (KMC) studies to elucidate the role of nonisothermal coalescence in tailoring the size and shape of nanoparticles generated via collision-coalescence events.[15]

The aforementioned studies have encouraged systematic characterizations of complex fractal-like structures of nanoaggregates, in lieu of the commonly used equivalent spherical shapes.[20,21] Such modifications significantly alter the inter-particle collision frequency function[22] and, hence, their growth dynamics. The excess surface area of fractal-like nanostructures, when coupled with the exothermic nature of coalescence, makes the chemical physics of surface energy driven interfacial processes such as oxidation and coagulation-coalescence in nanoparticles[23] highly complex and intriguing. Yet, to date a comprehensive study of the nonlinear coupling between all of the aforementioned energetic processes in the framework of synthesizing fractal-like nanostructures has not been performed.

Understanding these complex energetic processes is essential for establishing the process guidelines for synthesis of tailored nanostructures with controlled oxide layers for surface passivation, energetic or, specific catalytic and electronic applications[24–26]. Specifically, the energetic properties of metal nanoparticles (< 100 nm) with large surface-to-volume

Correspondence concerning this article should be addressed to D. Mukherjee at dmukherj@utk.edu.
Current Address of Matthew Wang: Dept. of Chemical and Biological Engineering, University of Wisconsin, Madison, WI 53706.

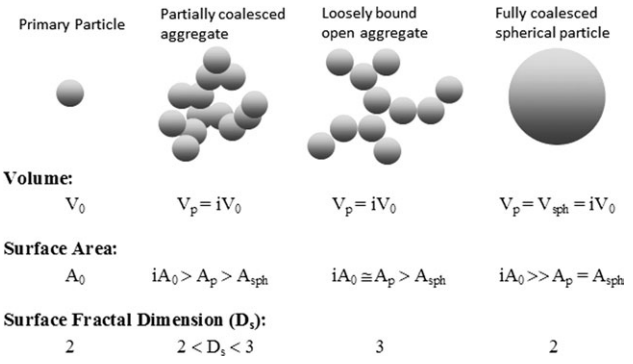

Figure 1. Schematic for qualitative definition of particle morphology variations.

ratio and energy densities[27–29] have attracted much attention from the combustion community (e.g., solid propellant or pyrotechnique research). To this end, oxidation kinetics of Al nanopowders have been investigated using thermogravimetric analysis (TGA), Rutherford backscattering spectrometry (RBS) studies,[30] single-particle mass spectrometry (SPMS),[31] and laser-induced breakdown spectroscopy (LIBS)[32] techniques.

Recent phenomenological models[33] and molecular dynamics (MD) simulations,[34,35] although simplistic in assuming spherical particle shapes, have provided critical insight into metal nanoparticle oxidation. However, due to computational limitations, they fail to account for the exothermic effects of the competing collision-coalescence processes during nanoparticle growth mechanism.[15] The motivation behind this investigation stems from the fact that most studies on metal nanoparticle oxidation rely on the simplified assumption of spherical particles, while looking at size evolution and/or surface oxidation of single particle,[33] uniformly sized particles[36] or ensemble particle-size distributions.[37] In this study, we have developed an efficient KMC model to account for coagulation-coalescence events coupled with particle energy balance and surface oxidation that leads to fractal-like structures for metal nanoparticles synthesized under typical processing conditions dictated by background gas pressure (p_g), temperature (T_g), and material volume loading (ϕ). This model for the first time allows investigation of the role of morphological complexity defined by surface fractal dimensions of metal nanoaggregates in their growth mechanism, energetic activities, extents of oxidation and structural/compositional changes. Specifically, due to the wealth of high-quality experimental data,[27–32] we have chosen to investigate gas-phase synthesis of Al nanoparticles undergoing simultaneous oxidation (i.e., Al/Al_2O_3 system) as a case-study to demonstrate the efficacy of the KMC model.

Model Development

Morphology: surface fractal dimension

This study is focused on interfacial processes such as coalescence and surface oxidation, and, hence, uses the surface fractal dimension D_s[38] to describe particle morphology. Based on the scaling law relation[39] between particle surface area (A_p), and volume (V_p): $A_p \propto V_p^{D_s/3}$ for fractal-like surfaces, D_s is estimated from the slope of a linear fit to $\ln(A_p/A_0)$ vs. $\ln(V_p/V_0)$ for the ensemble particle system as per the normalized area-to-volume relationship with their primary particles[38]

$$\frac{A_p}{A_0} = \left(\frac{V_p}{V_0}\right)^{\frac{D_s}{3}} \tag{1}$$

Theoretically, $2 \le D_s \le 3$, where $D_s = 2$ represents perfect smooth spheres; $2 < D_s < 3$ represents self-similar fractal-like aggregates undergoing partial coalescence and $D_s = 3$ represents completely open-chained fractal aggregates (see Figure 1).

In using Eq. 1, it needs to be mentioned that the choice of initial monomers as primary particles in the system, as used earlier,[46] is not valid when collision-coalescence mediated growth ($\tau_f \ll \tau_{coll}$) generates significantly large, uniform spherical particles that act as the primary particles in newly formed aggregates. Hence, subject to a log-normal distribution of aggregates coalescing into uniform spherical particles (discussed later), log mean diameter of the particle ensemble is assigned as the characteristic primary particle dimension. At the onset of aggregation, the primary particle size estimated from the most recent particle ensemble is used for the D_s estimation of all future aggregates. In addition, the validity of Eq. 1 for $D_s > 2$ requires a substantial number of primary particles (> 10 - 20) in any cluster to minimize error arising from the spherical primary particle morphology ($D_s = 2$).

Collision kernel and characteristic collision time

From kinetic theory the collision kernel between two particles i and j of any shapes and cluster sizes, varying particle temperatures[15] and densities (due to compositional variations), is given as[38]

$$\beta_{ij} = \frac{1}{4}\left(\frac{8k_b}{\pi}\right)^{1/2}\left(\frac{T_i}{\rho_i V_i} + \frac{T_j}{\rho_j V_j}\right)^{1/2}\left[(s_i A_i)^{1/2} + (s_j A_j)^{1/2}\right]^2 \tag{2}$$

The surface area accessibility term s_i accounts for the fractal-like surface structures and is related to the cluster size, i and D_s such that[38]

$$s_i = (D_s - 2)\left(\frac{2}{i}\right)^{1-\chi} + (3 - D_s) \tag{3}$$

where, it is noted that when $D_s = 2$ for dense spheres, $s_i = 1$ and χ is experimentally determined to be 0.92 for typical nanoparticle aggregation.[40,41]

In terms of β_{ij} (Eq. 2) and aerosol self-preserving size distribution (SPD) theory[42] based nondimensional particle volumes $\eta_i = N_\infty V_i/\phi$ and size distributions $\psi(\eta_i) = N_i\phi/N_\infty^2$, rate of change in particle number concentration is given as

$$\frac{dN_\infty}{dt} = -\frac{a}{2}\Omega N_\infty^{5/2} I(\eta_i, \eta_j) \text{where}, I(\eta_i, \eta_j) = \int_0^\infty \int_0^\infty F(\eta_i, \eta_j)\Psi(\eta_i)\Psi(\eta_j)d\eta_i d\eta_j \tag{4}$$

and

$$F(\eta_i, \eta_j) = \left(\frac{1}{\eta_i} + \frac{1}{\eta_j}\right)^{1/2}\left[\eta_i^{\gamma/2}\left\{1 + \left(b\theta/a\right)\eta_i^{1-\chi}\right\}^{1/2} + \eta_j^{\gamma/2}\left\{1 + \left(b\theta/a\right)\eta_j^{1-\chi}\right\}^{1/2}\right]^2 \tag{4a}$$

Table 1. Numerical Values of the Integral $I(\eta_i, \eta_j)$ in Eq. 4 for $D_s \to 2$ and $D_s \to 3$

D_s	2.0	2.1	2.2	2.3	2.4	2.5	2.6	2.7	2.8	2.9	3.0	Mean
$I(\eta_i, \eta_j)$ $D_s \to 3$	6.739	6.702	6.657	6.624	**6.576**	**6.578**	**6.569**	**6.546**	**6.576**	**6.572**	**6.615**	**6.576**
$I(\eta_i, \eta_j)$ $D_s \to 2$	**6.624**	**6.576**	**6.578**	**6.569**	**6.546**	**6.576**	**6.572**	6.615	6.651	6.694	6.744	**6.577**

where

$$\Omega = \left(\frac{2k_b\overline{T}}{\pi\overline{\rho}\phi}\right)^{\frac{1}{2}}\left(\frac{A_0}{2^{\chi}\eta_0^{\gamma}}\right); \gamma = (D_s/3 + \chi - 1); a = (D_s - 2);$$
$$b = (3 - D_s); \theta = (2\eta_0)^{\chi-1}; \eta_0 = N_\infty V_0/\phi$$

The volume integral over the entire population in Eq. 4 justifies the use of an ensemble averaged particle density and temperature $\overline{\rho}$ and $\overline{T}$, whereas the statistical nature of the problem provides support for the use of D_s, obtained from the linear fit of Eq. 1 over the particle ensemble, to represent the surface morphology of individual particles.

Here $I(\eta_i, \eta_j)$, which has been numerically solved for homogeneous forms of $F(\eta_i, \eta_j)$ at different volume fractal dimensions[42] (D_f), becomes analytically intractable and numerically intensive due to the nonhomogeneous form of $F(\eta_i \ \eta_j)$ in Eq. 4a. Thus, asymptotic solutions of $\left\{1 + (b\theta/a)\eta_i^{1-\chi}\right\}^{1/2} \cong 1$ when $(b\theta/a) \ll 1$ $(D_s \to 2)$ and $\left\{1 + (b\theta/a)\eta_i^{1-\chi}\right\}^{1/2} \cong (b\theta/a)^{1/2}\eta_i^{1-\chi/2}$ when $(b\theta/a) \gg 1$ $(D_s \to 3)$ (Note: $(b\theta/a)$ ranges over several orders of magnitude, whereas $\eta_i^{1-\chi} \sim 0.5 - 1.0$) lead to the homogeneous forms of $I(\eta_i, \eta_j)$. Upon numerical integration, $I(\eta_i, \eta_j)$ converges to the average values ~6.576 and 6.577 over the respective ranges of $D_s = 2.4$–3.0, and $D_s = 2.0$–2.6 (see Table 1). Finally, using an average value of $I(\eta_i, \eta_j) = 6.577$ in Eq. 4, the characteristic collision time τ_{coll} (time taken by a particle to double its volume, and, hence, N_∞ to drop to $N_\infty/2$ via coagulation) in the respective D_s regimes is estimated from

$$\tau_{coll} = \frac{N_\infty^{(\gamma-3/2)}\left(1 - 0.5^{(\gamma-3/2)}\right)}{Ya(\gamma - 3/2)I(\eta_i, \eta_j)}$$

$$\text{for } D_s \to 3 (\text{approaching fractal}) \quad (5)$$

$$\tau_{coll} = \frac{N_\infty^{(\gamma-\chi-1/2)}\left(1 - 0.5^{(\gamma-\chi-1/2)}\right)}{Yb(\gamma - \chi - 1/2)\left(\frac{2V_0}{\phi}\right)^{\chi-1}I(\eta_i, \eta_j)}$$

$$\text{for } D_s \to 2 (\text{approaching sphere}) \quad (6)$$

where the intermediate coefficient $Y = -\frac{1}{2}\left(\frac{2k_b\overline{T}}{\pi\overline{\rho}\phi}\right)^{\frac{1}{2}}\left(\frac{A_0}{2^{\gamma}}\right)\left(\frac{\phi}{V_0}\right)^{\gamma}$

The final τ_{coll}, as constructed from Eqs. 5 and 6 in the respective particle morphology regimes of $D_s \to 2$ (earlier times), and $D_s \to 3$ (later times), exhibit the expected escalation in τ_{coll} at later stages due to larger collision cross sections of fractal-like aggregates.

Coalescence

Coalescence is approximated by the following surface area reduction rate[42]

$$\frac{dA_p}{dt} = -\frac{1}{\tau_f}\left(A_p - A_{sph}\right) \quad (7)$$

where the mean characteristic fusion time τ_f (i.e., time needed to reduce the excess agglomerate surface area, $(A_p - A_{sph})$ by 63%) is estimated from individual $\tau_{f(M)}$ and $\tau_{(MOx)}$ weighted by the respective volume fractions of the metal (M) and its oxide (MOx)

$$\tau_f = \tau_{f(M)}^{\varphi_M}\tau_{f(MOx)}^{\varphi_{MOx}} \quad (8)$$

to account for the predominant diffusion rates due to dynamical variations in the M and MOx composition within the particle. Depending on particle temperatures T_p, melting points $T_{m(x)}$ and physical states of material, individual $\tau_{f(x)}$ ($x = M$ or MOx) are calculated as (1) $\tau_{f(x)} = \frac{3k_bT_pn_x}{64\pi\sigma_{s(x)}D_{eff}}$ for grain boundary diffusion (solid-state sintering when $T_p < T_{m(x)}$[43]), where D_{eff} is the effective diffusion coefficient[15] ($m^2\ s^{-1}$) (refer to the notation list), and (2) $\tau_{f(x)} = \frac{\mu_x d_{p(eff)}}{2\sigma_{l(x)}}$ for viscous diffusion (molten state liquid sintering when $T_p \geq T_{m(x)}$[16]), where $d_{p(eff)} = 6V_p/A_p$ accounts for multiple sintering necks on one particle.[15]

$T_{m(x)}$ ($x = M$ or, MOx), being highly sensitive to particle sizes (d_p) at nanoscale is determined from the expression for size-dependent melting point of nanomaterials[44]

$$T_{m(x)}(d_p) = T_{b(x)}\left\{1 - \frac{4}{h_L\rho_{s(x)}d_p}\left[\sigma_{s(x)} - \sigma_{l(x)}\left(\frac{\rho_{s(x)}}{\rho_{l(x)}}\right)^{2/3}\right]\right\} \quad (9)$$

The respective thermochemical and physical properties used in Eq. 9 (explained in the notation list) are specifically reported in Table 2 for the Al/Al_2O_3 case-study.

Surface oxidation: transport model and species balance

The surface oxidation model has the following features (1) uniform oxide shell formation, based on the shrinking core-like model[45]; hence, the core shrinks in size while maintaining the same morphology (given by D_s) as the external particle surface (refer to the schematic in Figure 2), (2) only surface oxidation of solid and liquid material leads to solid oxide (ash) formation, (3) O_2 diffuses through the ash layer to oxidize the metal at shell-core interface (reaction front indicated in Figure 2), (4) molten metal from unreacted core diffuses in opposite direction through the ash layer to react with O_2 at particle surface (reaction front indicated in Figure 2), (5) pressure gradient in nanoparticle core opposing the inward diffusion of O_2 and resulting in rupturing or thinning of ash layer[33] is not considered, and (6) D_s driven shape parameter factors account for particle morphology.

The Damköhler number (Da) determines the relative roles of reaction ($Da \ll 1$) or diffusion limited ($Da \gg 1$) oxidation mechanisms. It is defined for reacting species ($m = O_2$ or, metal) diffusing through mediums ($n =$ gas film or, ash layer) as

Table 2. Thermochemical and Physical Properties of Al and Al_2O_3

Properties	Al[(Ref.)]	Al_2O_3[(Ref.)]
Solid density, $\rho_{s(x)}$ (kg/m^3)	2700[47]	3980[47]
Solid surface tension, $\sigma_{s(x)}$ (J/m^2)	1.14[47]	1.12[47]
Liquid density, $\rho_{l(x)}$ (kg/m^3)	2377[48]	2930[49]
Liquid surface tension, $\sigma_{l(x)}$ (J/m^2)	1.05[50]	0.64[49]
Molecular weight (g/mol)	27	102
Molar volume, v_{mol} (m^3/mol)	$1x10^{-5}$	$2.56x10^{-5}$
Heat of vaporization, h_v (kJ/mol)	294[47]	346.94[51]*
Latent heat of melting, h_L (kJ/mol)	10.7[47]	109[49]
Heat capacity, $c_{p(x)}$ [J/(kg°C)]	917[47]	775[47]
Bulk melting point, $T_{m(x)}$ (K)	933[47]	2327[47]
Viscosity, μ_X (Pa-sec)	$4.97x10^{-4}$ $[T_m/(T_p-T_m)]^{0.5714}$[52]	$(3.2x10^{-3})$ $\exp[4.32x10^4/(R_uT_p)]$[49]
Grain boundary diffusion coefficient, D_{GB} (m^2/s)	(α/δ) $\exp[-\beta/(R_uT_p)]$[47]	(α/δ) $\exp[-\beta/(R_uT_p)]$[47]
δ:grain boundary width = 0.5 nm	$\alpha = 3x10^{-14}$m^2/s; $\beta = 6x10^4$ J/mol	$\alpha = 3x10^{-3}$m^2/s; $\beta = 4.77x10^5$ J/mol
Saturated vapor pressure, p_{sat} (Pa)	$\exp(13.07-36373/T_p)$[33]	$101325.\ \exp(13.42-27320/T_p)$[53]
Other thermochemical properties:		
Enthalpy of reaction (kJ/mol)	2324[31]	
Temperature dependent surface tension (N/m)	$\sigma_{Al}(T_p) = 0.001\ [860-0.134(T_p-933)]$[54]	
Thermal conductivity of Al_2O_3, k_{ash} [W/(m-K)]		$\alpha + \beta\ \exp[-\gamma(T_p-\theta)]/[(T_p-\theta)+\varepsilon]$[55] $\alpha=5.85$; $\beta=15360$; $\gamma=0.002$; $\theta=273.13$
First-order reaction rate coefficient, k_f (m/sec)		
$d_p < 50$nm	$24.\ \exp[-31.8x10^3/(R_uT_p)]$	
50nm $< d_p <$ 100nm	$180.\ \exp[-56.9x10^3/(R_uT_p)]$[31]	
100nm $< d_p$	$(5.4x10^7)\ \exp[-174.6x10^3/(R_uT_p)]$	
	$\mathbf{O_2 \rightarrow Al_2O_3}$	$\mathbf{Al \rightarrow Al_2O_3}$
Heterogeneous diffusion coefficient (m^2/sec)	$D_{O_2\|Ash} = \alpha\ \exp[-\beta/(R_uT_p)]$ $\alpha = 1.72x10^{-9}$ m^2/sec; $\beta = 69.5$ J/mol[31]	$D_{Al\|Ash} = \alpha\ \exp[-\beta/(R_uT_p)]$ $\alpha = 2.8x10^{-3}$ m^2/sec; $\beta = 477.3$ J/mol[53]

*h_v (kJ/mol) for Al_2O formation is considered by assuming the pathway for Al_2O_3 evaporation as: $4/3Al + 1/3Al_2O_3 \rightarrow Al_2O(g) \rightarrow 2Al(g) + 1/2O_2(g)$[51]

$$Da_{(m|n)} = \frac{\tau_{diff(m|n)}}{\tau_{rxn}} \tag{10}$$

Characteristic reaction time τ_{rxn} for surface oxidation of nanoparticles is defined as

$$\tau_{rxn} = \frac{1}{\zeta_{sv} k_f(T, d_p)} \tag{11}$$

Where $\zeta_{sv} = A_p/V_p$ is surface-to-volume ratio (m^{-1}) and $k_f(T,d_p)$ [$\sim\alpha_{oxid}\ \exp\ (-E_{oxid}/(k_bT_p))$] is the temperature and size (based on Al nanoparticle oxidation studies in size regimes of: $<$ 50 nm, 50–100 nm and $>$ 100 nm[31]) dependent first-order reaction rate coefficient (see Table 2). Characteristic diffusion time $\tau_{diff(m|n)}$ for species, m diffusing through medium, *n* is defined as

$$\tau_{diff(m|n)} = \frac{1}{\zeta_{sv}^2 D_{m|n}} \tag{12}$$

In this study, the following oxidation routes are considered:

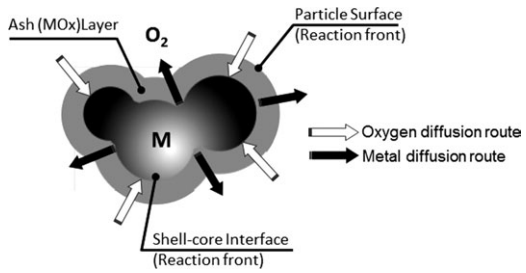

Figure 2. Schematic for shell-core oxidation model.

(a) *Bare metal particle: Diffusion of O_2 through the gas film*. For all cases studied, characteristic $Da_{(O_2|Gas)} \ll 1$ (where $\tau_{diff(O_2|Gas)}$ is determined from Eq. 12 using $D_{O_2|Gas}$[56]) for O_2 diffusion to the bare particle surface indicates the process to be always reaction controlled. Hence, the reaction rate is expressed as

$$\dot{\omega}_{O_2|Gas} = -\frac{dn_{O_2}}{dt} = A_p k_f C_{O,\infty} \tag{13}$$

(b) *Oxide coated particle*. Oxide shell formation prompts the following parallel processes: (1) *diffusion of O_2 through oxide shell to core surface*; net oxidation rate, mainly governed by the reaction at the *core metal surface* (Figure 2) is derived as

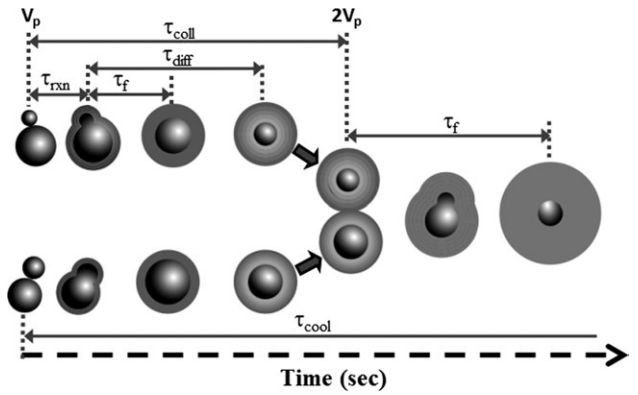

Figure 3. Schematic of the relative time scales of events during nanoparticle synthesis undergoing surface oxidation and simultaneous collision-coalescence processes where in for typical energetic oxidation processes $\tau_{cool} > \tau_{coll} > \tau_f > \tau_{diff} > \tau_{rxn}$

$$\dot{\omega}_{O_2|Ash} = -\frac{dn_{O_2}}{dt} = \frac{A_c k_f C_{O,\infty}}{1 + \frac{Da_{(O_2|Ash)}}{Z_{O_2}}} \quad (14)$$

and (2) *diffusion of molten metal through oxide shell to particle surface;* net oxidation rate, mainly governed by the reaction at the *particle surface* (Figure 2) is derived as

$$\dot{\omega}_{M|Ash} = -\frac{dn_M}{dt} = \frac{A_p k_f C_{M,c}}{1 + \frac{Da_{(M|Ash)}}{Z_M}} \quad (15)$$

Eqs. 14 and 15 are derived using the scaling law relations $A_p/A_c = \left(V_p/V_c\right)^{D_s/3}$ (self-similar shrinking core assumption in the aforementioned feature 1 and Figure 2) between the particle and its core-surface area and volume such that the morphological complexity are accounted for through the nondimensional shape parameters $Z_{O_2} = \sqrt{\frac{4\pi}{A_p}}\frac{\lambda^2}{\zeta_{sv}(\lambda-1)}$ (for O_2 diffusing out through the ash layer), and $Z_M = \frac{1}{\lambda^2}Z_{O_2}$ (for metal diffusing in through the ash layer) along with $\lambda = \left(V_p/V_c\right)^{D_s/6}$. The boundary conditions used for O_2 concentrations[45] in Eq. 14 are $C_O(A_p) = C_{O,\infty}$; $C_O(A_c) = 0$, while those for the metal concentrations in Eq. 15 are $C_M(A_c) = C_{M,c}$; $C_M(A_p) = 0$. Characteristic $Da_{(O_2|Ash)}$ (O_2 diffusion through the ash layer), and $Da_{(M|Ash)}$ (metal diffusion through the ash layer) are calculated from Eqs. 10 and 11 using the respective $\tau_{diff(O_2|Ash)}$ and $\tau_{diff(M|Ash)}$ (Eq. 12) as estimated from $D_{O_2|Ash}$ and $D_{M|Ash}$. It is noted that Eqs. 14 and 15, by their mechanistic design, shall drive the oxidation to be reaction limited or, diffusion limited based on the expressions $\frac{Da_{(O_2|Ash)}}{Z_{O_2}}$ and $\frac{Da_{(M|Ash)}}{Z_M}$ being $\gg 1$ or vice versa, respectively.

Specifically, for the Al/Al_2O_3 case-study used here to discuss the results obtained from this model, the extent of conversion α (i.e., the amount of Al converted to Al_2O_3) is defined as[31,32,45]

$$2Al + \frac{3}{2}\alpha O_2 \rightarrow (1-\alpha)Al + \alpha Al_2O_3 \text{ where,}$$

$$\alpha = \frac{2n_{Al_2O_3}}{2n_{Al_2O_3} + n_{Al}} \quad (16)$$

Finally, the stoichiometric species balance results in the net oxidation rate as

$$\dot{\omega}_{O_2} = \dot{\omega}_{O_2|Ash} + \frac{3}{4}\dot{\omega}_{Al|Ash} \quad (17)$$

Also, to account for compositional changes, mean particle density, ρ_p and surface tension, σ_p used throughout the simulations for the Al/Al_2O_3 system are estimated as

$$\rho_p = \varphi_{Al}\rho_{Al} + \left(1 - \varphi_{Al_2O_3}\right)\rho_{Al_2O_3}$$

$$\sigma_p = \varphi_{Al}\sigma_{Al} + \left(1 - \varphi_{Al_2O_3}\right)\sigma_{Al_2O_3}$$

where ρ_{Al} and $\rho_{Al_2O_3}$ are taken to be the bulk solid densities $\rho_{s(Al)}$ and $\rho_{s(Al_2O_3)}$, whereas surface tension of Al, σ_{A1} is calculated from $\sigma_{A1}(T_p)$, and $\sigma_{Al_2O_3}$ is taken as $\sigma_{s(Al_2O_3)}$ or, $\sigma_{l(Al_2O_3)}$ for $T_p < T_{m(Al2O3)}$ or vice versa, respectively (refer to Table 2).

Energy balance

The net rate of bulk energy increase E_p, in a nanoparticle/aggregate due to coalescence and oxidation, compensated by the rate of heat losses by conduction and evaporation (radiation being negligible in nanosized particles[15]) is given as

$$\frac{dE_p(T_p)}{dt} = \left(m_M c_{p(M)} + m_{MOx} c_{p(MOx)}\right)\frac{dT_p}{dt} = \dot{E}_{coal} + \dot{E}_{oxid} - \dot{E}_{cond} - \dot{E}_{evap} \quad (18)$$

Here $\dot{E}_{coal}$, based on coalescence rate (Eq. 7) for surface energy reduction, is given as[15]

$$\dot{E}_{coal} = -\sigma_p\frac{dA_p}{dt} = \frac{\sigma_p}{\tau_f}\left(A_p - A_{sph}\right) \quad (19)$$

$\dot{E}_{oxid}$ is calculated from oxygen consumption rate obtained from Eq. 17 as

$$\dot{E}_{oxid} = \dot{\omega}_{O_2}\frac{H^o_{rxn}}{N_{av}} \quad (20)$$

where $H_{rxn}{}^\circ$ is the enthalpy of metal oxidation (kJ mol^{-1}).

$\dot{E}_{cond}$ for the rate of heat loss via conduction is given as

$$\dot{E}_{cond} = \frac{R_{Kin}\left(T_p - T_g\right)}{\left(1 + \frac{R_{Kin}}{R_{Ash}}\right)} \quad (21)$$

where $R_{Ash} = k_{ash}\frac{\sqrt{4\pi A_p}}{\lambda - 1}$ is the resistance term for heat conduction through the ash layer, whereas $R_{Kin} = m_g c_g \frac{p_g A_p}{\sqrt{2\pi m_g k_b T_g}}$ accounts for collisions with gas molecules at the particle surface as derived from kinetic theory.[15] Here, the assumption of lumped heat in the metal core is valid for $c_{p(M)} > c_{p(MOx)}$.

Finally, $\dot{E}_{evap}$ for the rate heat loss via evaporation is formulated as

$$\dot{E}_{evap} = \frac{\varepsilon_{Kin}(h_v/N_{av})A_p}{\left(1 + \frac{\varepsilon_{Kin}}{\varepsilon_{Diff}}\right)} \quad (22)$$

where $\varepsilon_{Diff} = D_{M|Ash}C_{M,c}\frac{\sqrt{4\pi A_p}}{\lambda - 1}$ is the contribution from molten core metal diffusing through ash layer which competes with $\varepsilon_{Kin} = \frac{p_{drop}}{\sqrt{2\pi k_b T_p m_M}}$ due to evaporation of the molten metal from particle surface,[33] where vapor pressure on a droplet is related to that on a flat surface at temperature, T_p via Kelvin relation

$$p_{drop} = p_{sat}(T_p)\exp\left(\sqrt{\frac{\pi}{A_p}}\frac{4\sigma_p v_{mol}}{R_u T_p}\right) \quad (23)$$

For completely oxidized particles $\dot{E}_{evap}$ is calculated from the term ε_{Kin} only based on h_v, p_{drop} and p_{sat} of pure metal oxide. The temperatures ranges in this study makes oxide shell evaporation, although built into the model as a safeguard against exceedingly high-particle temperatures, negligible due to the fact that $T_{mp}(M) \ll T_{mp}(MOx)$, as well as p_{sat} being extremely low for most metal oxides. All thermochemical and physical properties used in the aforementioned equations for the simulation of Al/Al_2O_3 system in this study are charted out in Table 2. All notations used here are reported at the end of this article.

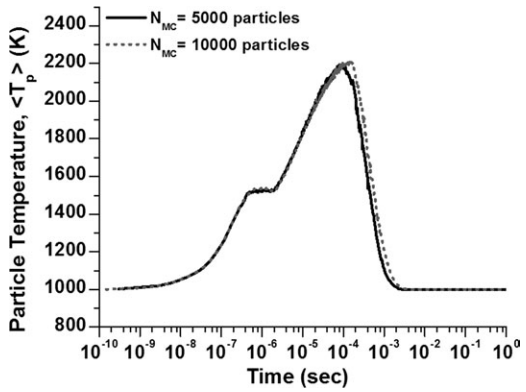

Figure 4. Temporal evolution of particle temperature (K) obtained from the MC runs N_{MC} = 5,000 and 10,000 particles showing the statistical accuracy of the results for the representative case-study of T_g = 1,000 K, p_g = 1 atm and $\phi = 10^{-6}$.

KMC model

This KMC model is built on an earlier coagulation driven constant-number (*constant-N*) MC model[15] with periodic boundary conditions,[46] wherein MC particles undergoing coagulation are replenished by replicating the system with copies of the surviving particles whenever the particle number drops to 50% of the initial number, thereby enabling a computationally efficient method without loss of accuracy. The probability of occurrence of a coagulation event in the KMC system is given as[15]

$$\mathrm{p_{ij}} = \frac{\beta_{\mathrm{ij}}}{\beta_{\max}} \tag{24}$$

wherein, as per Eq. 2, $\beta_{\max} = f(V_p, \rho_p, T_p, D_s)$ is estimated from all particles in the system. At any step, for $\mathrm{p_{ij}} \geq \mathrm{R} \in [0,1]$, a collision event between two randomly chosen particles (i and j) is accompanied by an advancement of the MC time-step $\Delta \mathrm{T_{MC}}$ (mean interevent time between successive coagulations) calculated from the inverse of the sum of the rates of all possible collision events[15]

$$\Delta \mathrm{T_{MC}} = \frac{2\mathrm{N_{MC}}}{\mathrm{N_\infty} \sum_{\mathrm{i}=1}^{\mathrm{N_{k-1}}} \sum_{\mathrm{j}=1}^{\mathrm{N_{k-1}}} \beta_{\mathrm{ij}}} \tag{25}$$

where, $\mathrm{V_{MC}} = \mathrm{N_{MC}}/\mathrm{N_\infty}$ is the MC volume represented in the system with number of simulation particles $\mathrm{N_{MC}}$.

Within each $\Delta \mathrm{T_{MC}}$, Eqs. 7, 13 (bare metal particles), or 17 (oxide coated particles), and 18 are numerically solved for coalescence, oxidation and energy/species conservations for the ensemble particles. The schematic in Figure 3 elucidates the characteristic time scales governing the interplay between the aforementioned processes, i.e., collision (τ_{coll}), fusion (τ_f), and diffusion (τ_{diff}) or, reaction (τ_{rxn}) limited oxidation in relation to the characteristic time taken to quench the energetic processes in a particle (τ_{cool}). To capture the real physicochemical processes, the rate-determining characteristic time, τ_{Char} is taken as the fastest among τ_{coll}, τ_f, τ_{diff} and τ_{rxn}, and it is used as the time step Δt within each ΔT_{MC} as

$$\Delta \mathrm{t} = \frac{\Delta \mathrm{T_{MC}}}{\mathrm{k_{max}}} \text{where,} \mathrm{k_{max}} = \frac{\Delta \mathrm{T_{MC}}}{\tau_{\mathrm{Char}}} \times \mathrm{k} \tag{26}$$

where $k_{\max}$ is the number of iteration loops for the numerical integrations ($k \sim 10$, or 100 to ensure accuracy). Typical particle temperature profiles obtained from simulations with N_{MC} = 5,000 and 10,000 show negligible variations (see Figure 4). Since the computational time for 5,000 particles is $\sim$3 days as compared to $\sim$3–5 weeks for 10,000 particles, all results presented, henceforth, are for N_{MC} = 5,000 particles.

Results and Discussion

All results presented here are for the representative case-study of the oxidation and evolution of $\mathrm{Al/Al_2O_3}$ nanoparticles during gas-phase synthesis.

Primary particle

For the estimation of the mean primary particle size, the particle ensemble is assumed to be "mostly spherical" when the ensemble averaged normalized excess surface area $\langle (\mathrm{A_p} - \mathrm{A_{sph}})/\mathrm{A_{sph}} \rangle < 0$. As an example, for T_g = 800 K, the primary particle size is fixed at $t = 7.52 \times 10^{-5}$ s when $\langle (\mathrm{A_p} - \mathrm{A_{sph}})/\mathrm{A_{sph}} \rangle > 0$ (Figure 5a) which corresponds to the crossing point between τ_f and τ_{coll} marking the onset of aggregation,[42] such that spherical particles formed for $\tau_f \ll$

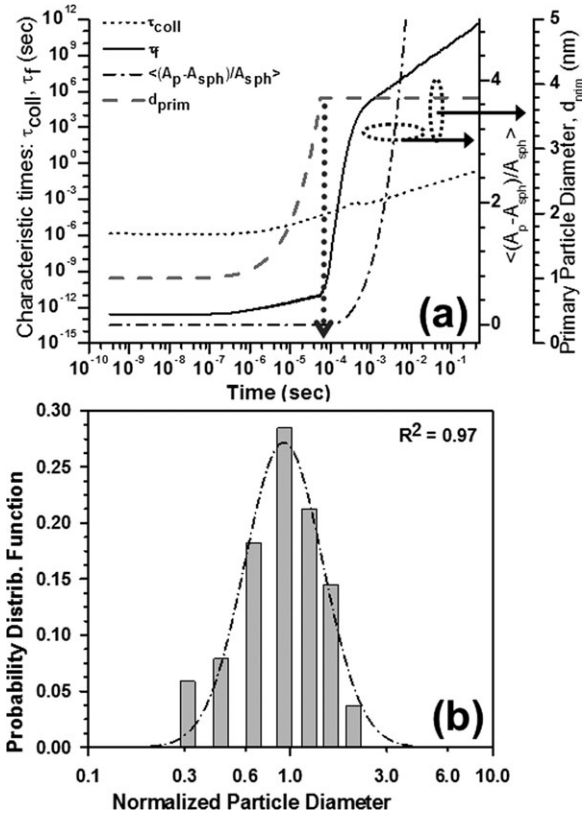

Figure 5. (a) Determination of primary particle size, d_{prim} (nm) when $\langle (\mathrm{A_p} - \mathrm{A_{sph}})/\mathrm{A_{sph}} \rangle \geq 0$ (t = 7.52 × 10^{-5} s), followed by the cross-over point of characteristic fusion (τ_f), and collision (τ_{coll}) times as indicated by the dotted arrow line, and (b) corresponding probability distribution function of primary particle sizes along with a peak fit indicating that the primary particles follow log-normal distribution with $\langle d_{\mathrm{prim}} \rangle \sim$3.8 nm, and σ_g = 1.93 (T_g = 800 K; p_g = 1 atm, and $\phi = 10^{-6}$).

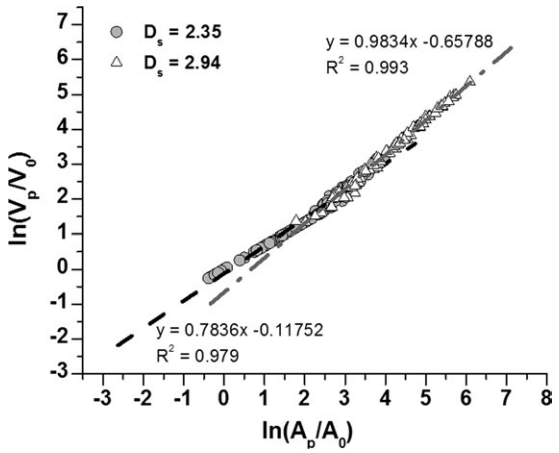

Figure 6. Typical plots of $\ln(V_p/V_0)$ vs. $\ln(A_p/A_0)$ indicating good linear fits used to determine D_s from their slopes as described by Eq. 3.

Representative case studied for $T_g = 800$ K, $p_g = 1$ atm and $\phi = 10^{-6}$.

τ_{coll} constitute the aggregates formed when $\tau_f > \tau_{coll}$ (collisions faster than coalescence). Keeping in mind that the slow approach of τ_f toward τ_{coll} ($d\tau_f/dt \ll d\tau_{coll}/dt$) at the crossing point might lead to the formation of oblong particles with long necks,[15] we strictly use $\langle (A_p - A_{sph})/A_{sph} \rangle > 0$ as the criterion for primary particle-size selection to ensure the choice of spherical primary particles only. Furthermore, due to periodic boundary conditions, sufficient collisions ensure a log-normal distribution for the uniform spherical particles formed before the onset of aggregation, beyond which the log-mean diameter of the most recent particle distributions is fixed as the primary particle size for the rest of the particle evolution study. This is corroborated by the probability distribution function of particle sizes in Figure 5b at $t = 7.5 \times 10^{-5}$ s (corresponding to $\langle (A_p - A_{sph})/A_{sph} \rangle \geq 0$ in Figure 5a), indicating a log-normal distribution with estimated log-mean diameters of $<d_{prim}> \sim 3.8$ nm ($\sigma_g = 1.93$), which is commensurate with $<d_{prim}>$ (marked on Figure 5a) used as the primary particle size (A_0, V_0) for the future particle evolution studies.

Particle morphology

Using A_0 and V_0 in Eq. 1, $D_s = 2.35$ and 2.94 at two different stages of particle evolution are estimated from the slopes of the two typical linear fits to $\ln(A_p/A_0)$ vs. $\ln(V_p/V_0)$ plots (Figure 6) for $T_g = 800$ K, $p_g = 1$ atm and$\phi = 10^{-6}$. The temporal variation of D_s in Figure 7 depicts the particle morphology evolution in relation to the different characteristic time scales τ_f, τ_{coll}, τ_{rxn} and $\tau_{diff(O2|Ash)}$ for the aforementioned operating conditions. Rapid coalescence at initial times, as compared to collision, oxidation due to surface reaction or, diffusion through the ash layer ($\tau_f \ll \tau_{coll}$, τ_{rxn} or $\tau_{diff(O2|Ash)}$), generates spherical particles ($D_s = 2$). However, hard oxide shell formation slows down self-diffusion, and, hence, coalescence. Thus, the particles transition from the molten viscous to the solid-state diffusion regime as τ_f rapidly crosses τ_{rxn} and $\tau_{diff(O2|Ash)}$ followed by τ_{coll}, hereby quenching the exothermic coalescence-oxidation processes. Corresponding to these crossing points D_s rapidly deviates from 2 (spheres) toward $D_s > 2$ (nonspherical), leading to aggregate formations ($D_s \sim 3$ at later stages in Figure 7). At lower T_g cases, surface oxidation due to extremely retarded metal diffusion through oxide layer is negligible.

Results for Al/Al$_2$O$_3$ evolution under different processing conditions

Simulation results are presented for processing conditions of (1) $T_g = 400$, 600, 1,000 and 1,400 K, (2) $p_g = 0.1$ and 1 atm, and (3) $\phi = 10^{-6}$ and 10^{-8} as encountered in typical laboratory or, industrial gas-phase synthesis of Al nanoparticles. Unless mentioned otherwise, all simulations are carried out with initial particle diam. $d_{ini} = 1$ nm in 5,000 particles system.

Effect of Gas Temperature (T_g). In contrast to the previous coalescence studies,[15] the nonlinear energetic coupling between coalescence and oxidation is manifested here through the drastic rise in mean particle temperature $<T_p>$ for $T_g = 400$ K, giving rise to the unique bimodal temperature profiles for $T_g = 1{,}000$ and 1,400 K (Figure 8a). An early rise in $<T_p>$ (bold arrow in Figure 8a) is followed by a subsequent reduction and the formation of a second peak that finally equilibrates to T_g. In early stages, higher T_g promotes thermally activated processes such as (1) nonisothermal coalescence due to competing collision-coalescence events ($\tau_f \ll \tau_{coll}$ in Figure 8b), and (2) O_2 and molten Al (in this case) diffusion through relatively thin oxide layers. Specifically, when $<T_p> > 1{,}000$ K, enhanced Al diffusion promotes rapid oxidation leading to hard oxide shell formation which, in turn, retards coalescence and results in the temporary reduction of $<T_p>$. However, the oxide shell insulation also retards conductive and evaporative heat losses from the Al core which, for small cluster sizes ($d_{prim} = 4.7$ and 8.4 nm for $T_g = 1{,}000$ and 1,400 K, respectively from Figure 8b), activate a second heat release mechanism dominated by the combined metal-metal oxide sintering (Figure 8a and $\tau_f \ll \tau_{coll}$ in Figure 8b). Thick oxide shells hinder both Al and O_2 diffusion and quench coalescence ($\tau_f > \tau_{coll}$ in Figure 8.b) through the final oxidation stages. Eventually, fractal-like structures with large surface-to-volume ratio ζ_{SV} (Figure 9) promote evaporative and conductive heat losses that relax $<T_p>$ back to T_g.

In relation to the sequence of aforementioned events, the morphological evolution (Figure 9a) indicates that increasing T_g delays the cross-over points between τ_f and τ_{coll} (Figure 8b). This concurs with the formation of nonspherical clusters ($D_s > 2$) with larger d_{prim} (Figure 8b), and lower ζ_{SV} (Figure

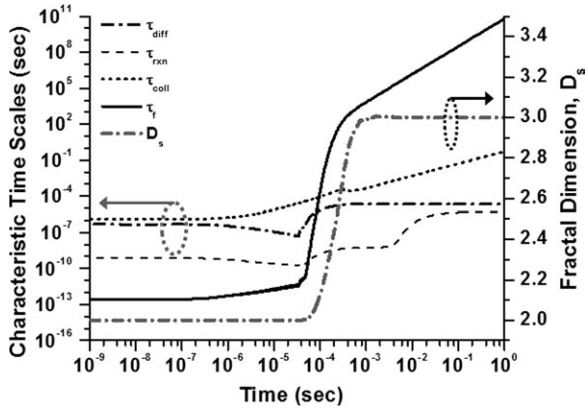

Figure 7. Temporal evolution of typical characteristic times τ_f, τ_{coll}, τ_{rxn} and $\tau_{diff(O2|Ash)}$, and the significance of their cross-over points with respect to the fractal dimension, D_s evolution for nanoparticles studied at $T_g = 800$ K; $p_g = 1$ atm and $\phi = 10^{-6}$.

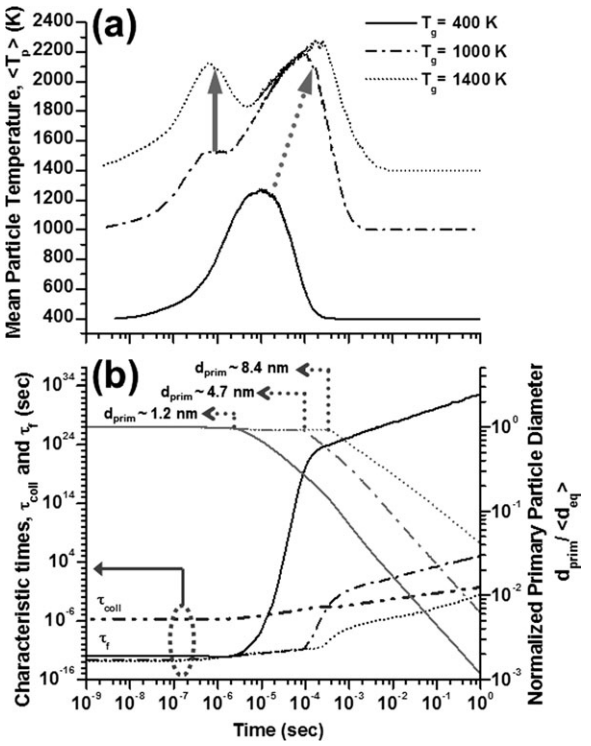

Figure 8. Temporal variation of (a) mean particle temperatures $<T_p>$, and (b) characteristic collsion (τ_{coll}), fusion (τ_f) times (black lines; left Y-axis), and primary particle diameters normalized by volume equivalent diameters $d_{prim}/<d_{eq}>$ (gray lines; right *y*-axis) for T_g = 400, 1,000 and 1,400 K (p_g = 1 atm and $\phi = 10^{-6}$).

Corresponding d_{prim} values when $d_{prim}/<d_{eq}> > 1$ for each of the T_g cases are indicated.

9a). While an earlier onset of fractal-like structures ($D_s > 2$) coincides with the peak in $<T_p>$ for T_g = 400 K, particles continue to coalesce into spheres ($D_s = 2$), until the second peak in $<T_p>$ (Figure 9a) for T_g = 1,000 and 1,400 K. Finally, fractal-like aggregates ($D_s = 3$) form to reduce ζ_{SV} to a constant lower bound value except for T_g = 1,400 K, where $d\tau_f/dt \approx d\tau_{coll}/dt$ (see Figure 8b) promotes the formation of partially sintered nonspherical particles ($D_s < 2.25$ in Figure 9a).

In Figure 9b, the extent of oxidation, α for T_g = 400 K indicates that spherical particles ($D_s = 2$) oxidize until 4×10^{-6} s (Figure 9a) to form a critical shell ($\alpha = 0.3$ in Figure 9b), beyond which partially sintered nonspherical particles with excess surface area (D_s ~2–2.5 in Figure 9a) drive α to a maximum ($\alpha = 0.59$ and $d\alpha/dt \approx 0$ in Figure 9b). However, for T_g = 1,000 and 1,400 K, subsidence of the first peak in $<T_p>$ (Figure 8a) in unison with $\alpha = 0.3$ (Figure 9b) indicates surface oxidation as the dominant exothermic contributor until this point. In the later stages, the formation of spherical particles ($D_s = 2$) until $\sim 10^{-4}$ s (Figure 9a) implies a dominant coalescence (as discussed earlier), wherein most of the oxidation (> 85%) has already ensued (Figure 9b). Eventually, nonspherical particles (D_s ~2– 2.5) attain the maximum α and fractal-like structures ($D_S = 3$) at later times ($> 10^{-4}$ s) for T_g = 1,000 K. In contrast, for T_g = 400 K, the particles continue to exhibit a steady rise in α (Figure 9b). The inflexion at $\alpha = 0.3$ (inset in Figure 9b and prominent for T_g = 1,400 K) separates the two energetic regimes: (1) thermally controlled oxidation prompting higher α with increasing T_g before the critical oxide shell formation, and (2) morphologically controlled oxidation beyond this point, wherein nonspherical particles for T_g = 400 K (D_s = 2–2.5 from Figure 9 and $<T_p> > 1{,}000$ K from Figure 8a) attain higher α than those for the other T_g ($D_s = 2$ until $\sim 10^{-4}$ s from Figure 9a, while $<T_p> > 1{,}200$ K from Figure 8a). This is specifically exemplified by the T_g = 1,400 K case (Figure 9b).

To probe into the roles of classical oxidation mechanisms, Figure 10 compares residence times from KMC simulations (t_{MC}) with those for typical reaction ($t_{Reaction}$), and diffusion ($t_{Diffusion}$) limited processes theoretically determined based on characteristic times for complete conversion via diffusion ($T_{Diffusion}$), or reaction ($T_{Reaction}$) as[45]

$$\frac{t_{Reaction}}{T_{Reaction}} = 1 - (1-\alpha)^{1/3}; T_{Reaction} = \frac{\rho_{mol(Al)} d_p}{(8/3) k_f C_{O,\infty}} \quad (27a)$$

$$\frac{t_{Diffusion}}{T_{Diffusion}} = 1 - 3(1-\alpha)^{2/3} + 2(1-\alpha);$$

$$T_{Diffusion} = \frac{\rho_{mol(Al)} d_p^2}{32 D_{O_2|Ash} C_{O,\infty}} \quad (27b)$$

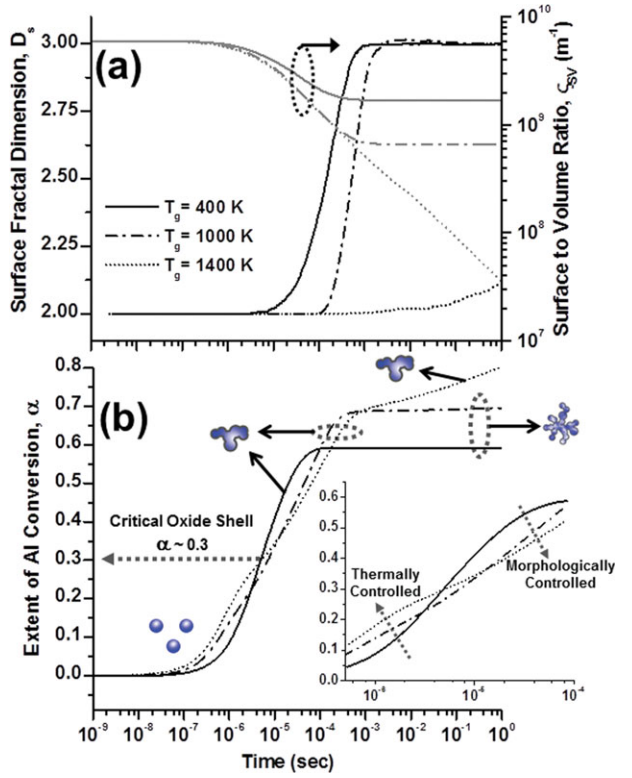

Figure 9. Temporal variation of (a) surface fractal dimension, D_s (black lines; left *y*-axis); surface-to-volume ratio, ζ_{SV} (gray lines; right *y*-axis), and (b) extents of Al conversion, α in particles synthesized at T_g = 400, 1,000 and 1,400 K (p_g = 1 atm and $\phi = 10^{-6}$).

Schematics indicate corresponding morphology during different stages of particle evolution. (Inset: Blow-up of α around the inflexion point, i.e., critical oxide shell, $\alpha \sim 0.3$). [Color figure can be viewed in the online issue, which is available at wileyonlinelibrary.com.]

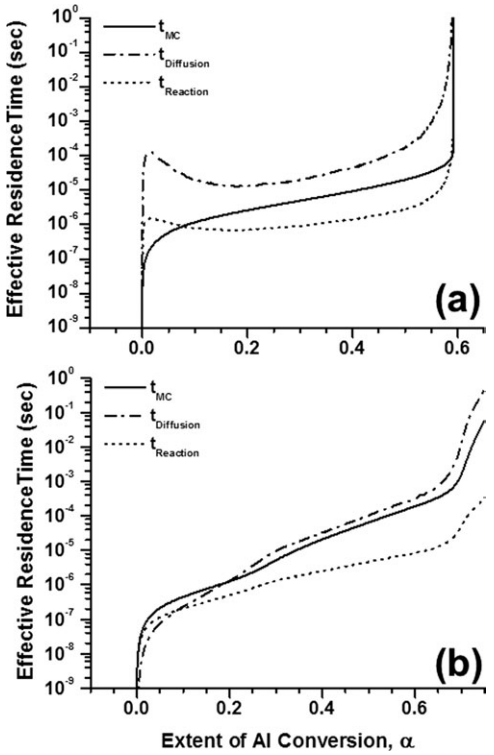

Figure 10. Variation of theoretical effective residence time for reaction ($t_{Reaction}$) and diffusion ($t_{Diffusion}$) limited oxidation mechanisms as calculated from Eqs. 27a and b compared to the KMC simulation residence time (t_{MC}) as a function of extent of conversion α for: (a) T_g = 400 K, and (b) T_g = 1,400 K (p_g = 1 atm and $\phi = 10^{-6}$).

where, $\rho_{mol(Al)}$ is the molar density of Al (mol m^{-3}). For T_g = 400 K, unlike common nanoparticle oxidation models,[31,33] the mechanism starts off as reaction-limited, but shifts between diffusion and reaction limited regimes (morphology controlled) as the particle evolves whereas for T_g = 1,400 K, immediately after the initial oxide shell formation, t_{MC} uniformly follows the diffusion-limited mechanism trend (thermally activated with dominant coalescence), leading to continuous increase in α as discussed earlier.

Effect of Gas Pressure (p_g). With decreasing p_g, the lack of gas molecules to facilitate the heat dissipation from nanoparticles[15] promotes an enhanced energetic behavior as indicated by the activated rise in $<T_p>$ (Figure 11a for relatively low T_g = 600 K). Figure 11a indicates the familiar monomodal profile for p_g = 1 atm and a strong bimodal profile (similar to earlier high T_g cases) for p_g = 0.1 atm. For p_g = 0.1 atm, the first peak is a result of nonlinear coupling between uninhibited exothermic coalescence (weaker conduction heat losses due to fewer gas molecule collisions between successive particle collisions), and oxidation driven by the enhanced metal and oxygen diffusion through ash layer. As described earlier, a temporary retardation in coalescence due to oxide shell formation lowers the $<T_p>$ en route to its second peak due to the sintering of oxide coated small particles (d_{prim} < 12 nm in Figure 11c). Specifically, for p_g = 0.1 atm, the second peak in $<T_p>$ (~2,300 K) concurs with the melting point of Al_2O_3 (= 2,327 K), wherein activated evaporative heat losses initiate the relaxation of $<T_p>$. This upper limit of the second peak in $<T_p>$, as consistently noted earlier (Figure 8a) for T_g = 400 as well as T_g = 800 K at p_g = 0.1 atm (not shown here), enforces an upper bound for ignition temperatures once oxide shells are formed.

Despite the higher $<T_p>$ for p_g = 0.1 atm, Al nanoparticles indicate a higher α = 0.74 for p_g = 1 atm as compared to α = 0.5 for p_g = 0.1 atm (Figure 11a). This can be rationalized based on the particle morphology evolution. For both p_g = 0.1 and 1 atm, rapid oxidation in fully coalesced ($\tau_f \ll \tau_{coll}$ in Figure 11c) spherical nanoparticles (D_s = 2

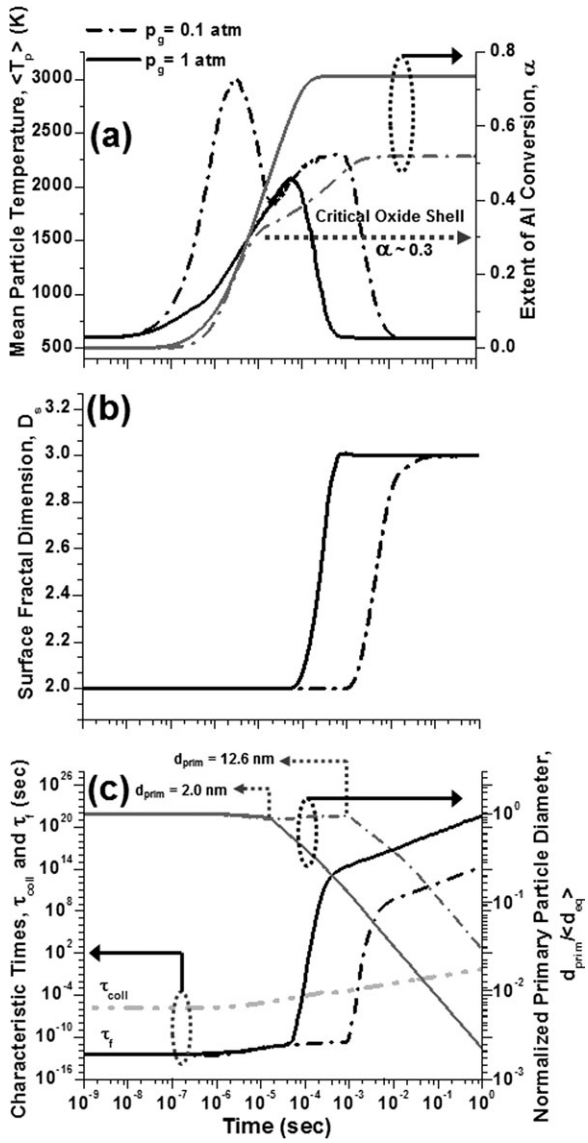

Figure 11. Temporal variation of (a) mean particle temperature, $<T_p>$ (black lines; left *y*-axis), extents of Al conversion, α (gray lines; right Y-axis), (b) surface fractal dimension D_s, and (c) characteristic collision (τ_{coll}; gray dash dot-dot line), fusion (τ_f; all black lines) times (left *y*-axis) and $d_{prim}/<d_{eq}>$ (gray lines; right *y*-axis) for p_g = 0.1 and 1 atm (T_g = 600 K and $\phi = 10^{-6}$).

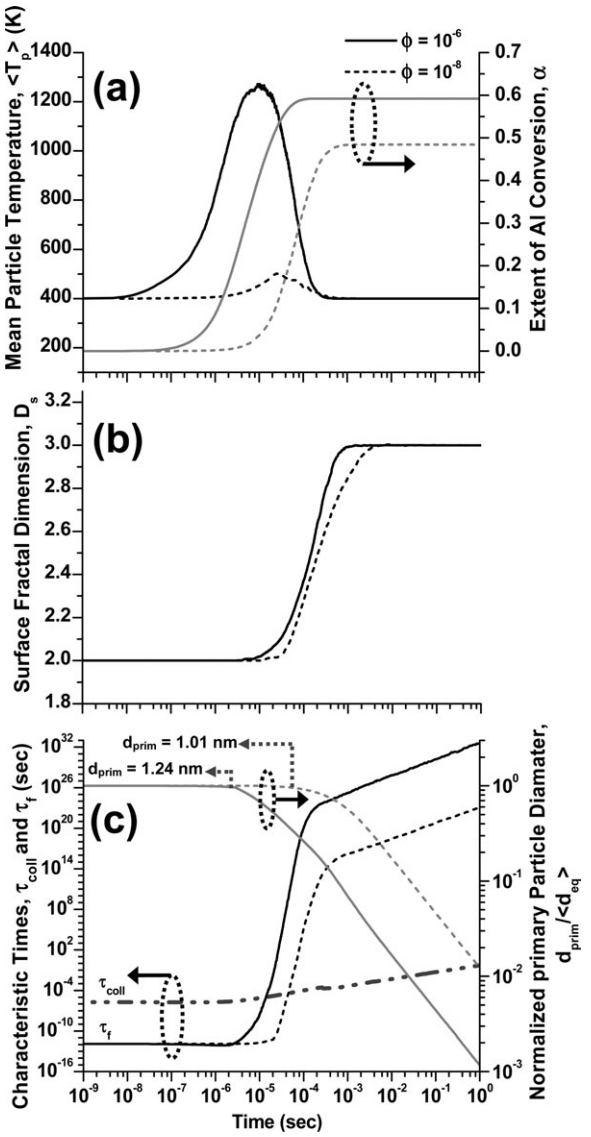

Figure 12. Temporal variation of (a) mean particle temperature $<T_p>$ (black lines; left y-axis) and extents of Al conversion, α (gray lines; right *y*-axis), (b) surface fractal dimension D_s, and (c) characteristic collision (τ_{coll}; gray dash dot-dot line), fusion (τ_f; all black lines) times (left Y-axis) and $d_{prim}/<d_{eq}>$ (gray lines; right *y*-axis) for $\phi = 10^{-6}$ and 10^{-8} ($T_g = 400$ K and $p_g = 1$ atm).

until 6×10^{-5} and 10^{-3} s, respectively, in Figure 11b) forms the critical oxide shell ($\alpha = 0.3$ in Figure 11a). At this point, the inflexion in α for $p_g = 0.1$ atm coincides with subsidence in the first peak of $<T_p>$. Beyond this point, oxidation rate for fully sintered spherical particles ($\tau_f \ll \tau_{coll}$ in Figure 11c and $D_s = 2$ till $\sim 10^{-3}$ s in Figure 11b) for $p_g = 0.1$ atm is distinctly retarded (see Figure 11a) as compared to that for $p_g = 1$ atm due to the available excess surface area ($D_s > 2$ in Figure 11b) of partially coalesced (τ_f approaching τ_{coll} in Figure 11c) nonspherical particles at relatively elevated $<T_p>$ (Figure 11a) in the latter case. Beyond 10^{-3} and until 6×10^{-3} s a slight increase in $d\alpha/dt$ for $p_g = 0.1$ atm, owing to the second peak in $<T_p>$ and nonspherical particle morphology ($D_s > 2$), is rapidly thwarted by significant oxidation on relatively large particles. Finally, α reaches its respective maximum values as $\tau_f > \tau_{coll}$, and $D_s = 3$. Furthermore, smaller $d_{prim} = 2.0$ nm for $p_g = 1$ atm as compared to $d_{prim} = 12.6$ nm for $p_g = 0.1$ atm (Figure 11c) suggests that exothermic coalescence and particle morphological complexity have significant impact on the oxidation behavior of smaller sized nanoclusters (< 10 nm). It needs to be mentioned that results for $p_g = 10$ atm (not shown here), despite large O_2 partial pressure, indicated minimal oxidation ($\alpha = 0.06$) in conjunction with negligible $<T_p>$ rise.

Effect of Volume Loading (ϕ). At $p_g = 1$ atm and $T_g = 400$ K, Al nanoparticles with volume loadings of $\phi = 10^{-6}$ exhibit a higher energetic behavior than that for $\phi = 10^{-8}$ which shows a minimal rise in $<T_p>$ (Figure 12a). In conjunction with this, for $\phi = 10^{-8}$, the formation of nonspherical particles ($D_s > 2$ in Figure 12b), and τ_f approaching τ_{coll} (Figure 12c) concur with the initiation of particle oxidation ($\alpha > 0$ in Figure 12a), beyond which α continuously

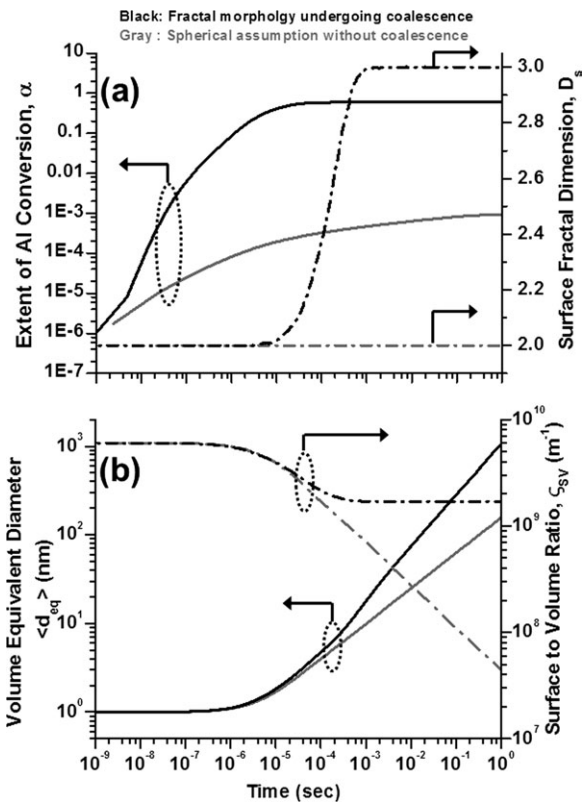

Figure 13. KMC simulations comparing temporal variations of (a) extents of conversion, α (solid lines on left *y*-axis) and surface fractal dimension D_s (dash-dot lines on right *y*-axis), and (b) volume equivalent dia. $<d_{eq}>$ (solid line on left *y*-axis), and surface-to-volume ratio, ζ_{SV} (dash-dot line on right *y*-axis) ($d_{ini} = 1$ nm, $T_g = 400$ K, $p_g = 1$ atm, and $\phi = 10^{-6}$) for particles undergoing exothermic coalescence mediated morphological evolution (all black lines), and particles assumed to be spherical without any coalescence (all gray line).

increases to a maximum ($\alpha = 0.48$) as the particles approach complete fractal like structures ($D_s = 3$). In contrast, for $\phi = 10^{-6}$ particles attain nonspherical shape ($D_s > 2$ in Figure 12b, and τ_f approaching τ_{coll} in Figure 12c) only at the onset of critical oxide shell formation ($\alpha \sim 0.3$ in Figure 12a), beyond which partial fractal-like structures ($D_s \sim 2$–2.5) undergo the maximum conversion ($\alpha \sim 0.59$). Thus, armed with relatively weak $<T_p>$, the particle evolution and relatively weaker oxidative processes for $\phi = 10^{-8}$ are driven by competing collision-coalescence processes, and, hence, largely morphologically controlled. This, in turn, implies that the benefit from morphology mediated nanoparticle oxidation is significantly enhanced in the presence of large thermal activation. Thus, earlier attainment of fractal-like structures for $\phi = 10^{-6}$ (D_s being higher than those for $\phi = 10^{-8}$ at any instance in Figure 12b) reflects in the respective α being consistently much higher for $\phi = 10^{-6}$ (Figure 12a). It needs to be highlighted here that, despite a relatively weak $<T_p>$ rise for $\phi = 10^{-8}$, the significant increase in α would not have been possible if fractal-like morphology of nanoparticles was not accounted for (discussed in the next section). Also, despite the crossing points between τ_f and τ_{coll} being earlier for $\phi = 10^{-6}$, the enhanced collisions from higher particle number density results in relatively larger $d_{prim} = 1.24$ nm for $\phi = 10^{-6}$ as compared to $d_{prim} = 1.01$ nm for $\phi = 10^{-8}$ (Figure 12c). This reiterates the idea that while weak thermally activated processes prompt nanoparticle morphological complexity to play important role in tuning their reactivity, a stronger presence of the former process significantly boosts their energetic behavior.

Implications of Coalescence Mediated Fractal like Morphology. The unique contribution of this study is highlighted by comparing results for Al nanoparticle oxidation starting with an initial diameter $d_{ini} \sim 1$ nm at $T_g = 400$ K, and $p_g = 1$ atm, while accounting for (1) exothermic coalescence mediated morphological evolution of nonspherical nanoparticles generated via collision-coalescence mechanisms, and (2) no morphological variations or, exothermic coalescence under the assumption of instant coalescence of colliding particles into spheres. As seen from Figures 13a and b for $T_g = 400$ K, as particles in case 1 evolve from spherical shapes ($D_s = 2$) into fractal-like structures ($D_s = 3$), the extents of oxidation, α for case 1 is significantly higher than that for case 2 (black lines for case 1, and gray lines for case 2). In conjunction to this, final ζ_{SV} (Figure 13b) for particles with complex morphology and larger surface area (case 1) is significantly higher than that for spherical particles (case 2), thereby supporting the enhanced α for case 1. Moreover, in case 1 the onset of fractal-like aggregates ($D_s > 2$ in Figure 13a) generates particles with larger volume equivalent diameters $<d_{eq}>$ (Figure 13b) as compared to their instantly coalesced spherical counterparts. It is noted that for case 1 significant amount of oxidation ($\alpha \sim 0.59$) ensues in the size regime of $<d_{eq}> < 10$ nm ($t \sim 10^{-4}$ s.). Enhanced coalescence mediated thermal activities in spherical particles dominate the early stages until $<d_{eq}> \sim 1.5$ nm ($t \sim 4 \times 10^{-6}$ s) beyond which, until $<d_{eq}> \sim 10$ nm ($t \sim 10^{-4}$ s), coalescence mediated nonspherical morphology drives the final stages of particle oxidation, i.e, $\alpha \sim 0.3$–0.59 as $D_s \sim 2$–2.5 (as discussed earlier). In comparison, case 2 shows much slower and yet, continuous rise all through its evolution, regardless of particle size or morphology.

Conclusion

A high-fidelity coagulation driven KMC model has been developed to study the impact of fractal-like morphology on the oxidation behavior of metal nanoparticle aggregates evolving via collision-coalescence mediated energetic processes under different processing conditions of background temperature (T_g), pressure (p_g), and material volume loading (ϕ). Simulation results, as exemplified by the Al/Al_2O_3 system, reveal that a complex nonlinear coupling between nonisothermal coalescence and surface oxidation, while generating nonspherical/fractal like structures, manifest a bimodal particle temperature profile under high T_g and low p_g conditions. The first bout of heat release is temporarily abated by the formation of critical oxide shell ($\alpha \sim 0.3$) which acts as an insulation against core heat losses to prompt the second heat release through thermally activated coalescence of the metal/metal oxide (Al/Al_2O_3 in this case) nanostructures. This self-enforcing heat release is finally quenched by the formation of large fractal-like particle structures and an upper bound of the high melting point of metal oxides (specifically, $\sim$2327 K for Al_2O_3). For relatively low T_g ($\sim$400– 600 K), and high p_g conditions, the commonly observed monomodal particle temperature profile drives the process through (1) thermally controlled oxidation till the critical shell formation, beyond which (2) morphologically controlled oxidation sets in, wherein nonspherical particles with excess area ($D_s = 2$–2.5) and $<T_p> > 1{,}000$ K give rise to enhanced oxidation in comparison to their spherical particle counterparts evolving under high T_g and low p_g conditions.

Present simulations elucidate the role of process parameters (T_g, p_g, ϕ) in tailoring the energetic properties of metal/metal oxide nanostructures generated via gas phase synthesis. High T_g, low p_g and low ϕ conditions produce relatively uniform structures with extensive oxidation and spent core energy whereas, intermediate $T_g > 600$ K with high p_g and high ϕ conditions lead to highly fractal-like structures with thin oxide shells that passivate the surface to preserve energetic properties of the metal aggregates. Specifically, simulation results accounting for nonisothermal coalescence in fractal-like particle morphology, when compared to those obtained with the assumption of instantly coalescing spherical particles, reveal the significant impact of the former case on surface oxidation of nonspherical metal nanoparticles (specifically in the size ranges of $<$ 10–15 nm).

Acknowledgments

This work was supported by funding from Material Research and Innovation Laboratory (MRAIL) at University of Tennessee, Knoxville.

Notation

A_0 = primary particle surface area, m^2
A_c = core-surface area at the shell-core interface, m^2
A_p, A_i, A_j = surface area of particle/aggregates with cluster sizes i, j, m^2
A_{sph} = surface area of volume equivalent spherical particle, m^2
c_g = specific heat capacity of gas (air), J kg^{-1} K^{-1}
$c_{p(x)}$ = specific heat capacity of x = Al, or Al_2O_3 in the particle
$C_{O,\infty}$ = number concentrations of free stream O_2 molecules, # m^{-3}
$C_{M,c}$ = number concentrations of metal atoms in particle core, # m^{-3}
D_{eff} = effective solid-state diffusion coefficient, m^2 s^{-1}: $D_{eff} = D_{GB}\left(\frac{\delta}{d_{p(small)}}\right)$
D_s = surface fractal dimension
D_{GB} = grain boundary self-diffusion coefficient (m^2 s^{-1}) as reported in Table 2

$D_{m|n}$ = heterogeneous diffusion coefficient of m = O_2 or, Al in n = Ash/Al_2O_3 as reported in Table 2
$Da_{(m|n)}$ = Damköhler number for m = O_2 or, metal diffusion in n = gas film, or metal oxides
d_p = volume equivalent particle diameter, m
$d_{p(eff)}$ = effective diameter of particle such that $d_{p(eff)} = 6V_p/A_p$
$d_{p(small)}$ = diameter of smallest coalescing particle in an aggregate[15]
h_v = heat of vaporization for metal or, metal oxides, kJ mol^{-1}
h_L = latent heat of melting for metal or, metal oxides, kJ mol^{-1}
H_{rxn}° = enthalpy of metal oxidation, kJ mol^{-1}
i, j = cluster sizes
k_{ash} = thermal conductivity of metal oxide, W m^{-1} K^{-1}
k_b = boltzmann's constant, 1.38×10^{-23}, J K^{-1}
k_f = first-order reaction rate coefficients, k_f (T,d_p), m sec^{-1}
m_g = mass of gas molecule, 4.8×10^{-26}, kg
m_x = mass of x = metal (M) or, metal oxide (MOx), kg
n_{O_2} = number of O_2 molecules
n_x = number of x = metal (M) atoms or, metal oxide (MOx) molecules in a particle
N_{av} = Avogadro's number, 6.02×10^{23}, # mol^{-1}
N_{MC} = Monte-Carlo number of particles
N_{∞} = total number concentration of particles, # m^{-3}
p_{drop} = vapor pressure on a droplet as given by Kelvin effect, Pa
p_g = background gas pressure, atm
p_{ij} = Monte-Carlo collision probability
p_{sat} (T_p) = saturated vapor pressure over flat surface at T_p
R_u = universal gas constant, 8.31, J mol^{-1} K^{-1}
s_i, s_j = surface area accessibility of cluster sizes i and j
$t_{Reaction}$, $t_{Diffusion}$ = effective residence times for reaction and diffusion limited processes, respectively
$T_{Reaction}$, $T_{Diffusion}$ = characteristic times for complete conversions via reaction or diffusion, respectively[45]
$\overline{T}$ = ensemble averaged particle temperature, K
T_g = background gas temperature, K
$T_{m(x)}$ = melting point for x = metal (M) or, metal oxide (MOx)
T_p, T_i, T_j = temperature of particles/aggregates with cluster sizes i and j, K
v_{mol} = molar volume of metal (M) or, metal oxide (MOx)
V_0 = primary particle volume, m^3
V_c = core volume, m^3
V_{MC} = Monte-Carlo volume space, m^3
V_p, V_i, V_j = volume of particles/aggregates with cluster sizes i and j, K

Greek symbols

α = extent of conversion (specifically, amount of Al converted to Al_2O_3)
β_{ij} = collision kernel or frequency function, m^3 s^{-1}
χ = surface area scaling factor[40]
δ = grain boundary width, m
ΔT_{MC} = Monte-Carlo time step, s
Δt = numerical integration time-step, s
ϕ = particle volume loading
$\eta_i\eta_j$ = nondimensional particle volume in SPD
ϕ_x = volume fractions of metal or, metal oxides, specifically, for x = Al or, Al_2O_3
λ = shape parameter expressed as $\lambda = \left(V_p/V_c\right)^{D_s/6}$
μ_x = viscosity of x = metal (M) or, metal oxide (MOx), Pa s
$\rho_{s(x)}$ = solid density of x = metal (M) or, metal oxide (MOx), kg m^{-3}
$\rho_{l(x)}$ = liquid density of x = metal (M) or, metal oxide (MOx), kg m^{-3}
$\rho_{mol(Al)}$ = molar density of Al, mol m^{-3}
ρ_p, ρ_i, ρ_j = mean density of particles/aggregates of cluster sizes i and j (kg m^{-3})
$\overline{\rho}$ = ensemble averaged particle density, kg m^{-3}
$\sigma_{s(x)}$ = solid surface tension for x = metal (M) or, metal oxide (MOx), J m^{-2}
$\sigma_{l(x)}$ = liquid surface tension for x = metal (M) or, metal oxide (MOx), J m^{-2}
$\sigma_{Al}(T_p)$ = temperature-dependent surface tension of Al (see Table 2), J m^{-2}
σ_p = mean particle surface tension, J m^{-2}
τ_f = mean characteristic fusion/coalescence time, s
$\tau_{f(x)}$ = characteristic fusion times for x = metal (M) or, metal oxide (MOx), s
τ_{coll} = characteristic collision time, s
$\tau_{diff(m|n)}$ = characteristic diffusion times for species, m diffusing in medium, n s
τ_{rxn} = characteristic reaction time for surface oxidation, s
$\dot{\omega}_{m|n}$ = oxidation rates at core (m = O_2) or, surface (m = M) where n = Ash (s^{-1})
$\dot{\omega}_{O_2}$ = net oxidation rate in particles, s^{-1}
$\Psi(\eta_i)$, $\Psi(\eta_j)$ = size distribution function in SPD
ζ_{SV} = surface to volume ratio of particles/aggregates, $\zeta_{SV} = A_p/V_p$ (m^{-1})

Literature Cited

1. Rosner DE. Flame synthesis of valuable nanoparticles: Recent progress/current needs in areas of rate laws, population dynamics, and characterization. *Ind Eng Chem Res* 2005;44(16):6045–6055.
2. Strobel R, Pratsinis SE. Flame aerosol synthesis of smart nanostructured materials. *J Mater Chem*. 2007;17(45):4743–4756.
3. Bapat A, Anderson C, Perrey CR, Carter CB, Campbell SA, Kortshagen U. Plasma synthesis of single-crystal silicon nanoparticles for novel electronic device applications. *Plasma Phys Contr Fusion*. 2004;46(Sp. Iss. SI Suppl. 12B):B97–B109.
4. Holunga DM, Flagan RC, Atwater HA. A scalable turbulent mixing aerosol reactor for oxide-coated silicon nanoparticles. *Ind Eng Chem Res*. 2005;44(16):6332–6341.
5. Kommu S, Wilson GM, Khomami B. A theoretical/experimental study of silicon epitaxy in horizontal single-wafer chemical vapor deposition reactors. *J Electrochem Soc*. 2000;147(4):1538–1550.
6. Gelbard F, Tambour Y, Seinfeld JH. Sectional representations for simulating aerosol dynamics. *J. Colloid Interface Sci*. 1980;76(2):541–556.
7. Prakash A, Bapat AP, Zachariah MR. A simple numerical algorithm and software for solution of nucleation, surface growth, and coagulation problems. *Aerosol Sci. Technol*. 2003;37(11):892–898.
8. Mukherjee D, Prakash A, Zachariah MR. Implementation of a discrete nodal model to probe the effect of size-dependent surface tension on nanoparticle formation and growth. *J Aerosol Sci*. 2006;37:1388–1399.
9. Frenklach M, Harris SJ. Aerosol dynamics modeling using the method of moments. *J. Colloid Interface Sci*. 1987;118(1):252–261.
10. Whitby ER, McMurry PH. Modal aerosol dynamics modeling. *Aerosol Sci. Technol*. 1997;27(6):673–688.
11. Kommu S, Khomami B, Biswas P. Simulation of aerosol dynamics and transport in chemically reacting particulate matter laden flows. Part I: Algorithm development and validation. *Chem Eng Sci*. 2004;59(2):345–358.
12. Garrick SC, Lehtinen KEJ, Zachariah MR. Nanoparticle coagulation via a Navier-Stokes/nodal methodology: Evolution of the particle field. *J Aerosol Sci*. 2006;37(5):555–576.
13. Efendiev Y, Zachariah MR. Hierarchical hybrid Monte-Carlo method for simulation of two-component aerosol nucleation, coagulation and phase segregation. *J Aerosol Sci*. 2003;34(2):169–188.
14. Maisels A, Kruis FE, Fissan H. Direct simulation Monte Carlo for simultaneous nucleation, coagulation, and surface growth in dispersed systems. *Chem Eng Sci*. 2004;59(11):2231–2239.
15. Mukherjee D, Sonwane CG, Zachariah MR. Kinetic Monte Carlo simulation of the effect of coalescence energy release on the size and shape evolution of nanoparticles grown as an aerosol. *J Chem Phys*. 2003;119(6):3391–3404.
16. Tandon P, Rosner DE. Monte Carlo simulation of particle aggregation and simultaneous restructuring. *J. Colloid Interface Sci*. 1999;213(2):273–286.
17. Tsantilis S, Pratsinis SE. Soft- and hard-agglomerate aerosols made at high temperatures. *Langmuir*. 2004;20(14):5933–5939.
18. Zachariah MR, Carrier MJ. Molecular dynamics computation of gas-phase nanoparticle sintering: A comparison with phenomenological models. *J Aerosol Sci*. 1999;30(9):1139–1151.
19. Lehtinen KEJ, Zachariah MR. Energy accumulation in nanoparticle collision and coalescence processes. *J Aerosol Sci*. 2002;33(2):357–368.
20. Wu MK, Friedlander SK. Enhanced power-law agglomerate growth in the free-molecule regime. *J Aerosol Sci*. 1993;24(3):273–282.
21. Maricq MM. Coagulation dynamics of fractal-like soot aggregates. *J Aerosol Sci*. 2007;38(2):141–156.
22. Zurita-Gotor M, Rosner DE. Effective diameters for collisions of fractal-like aggregates: Recommendations for improved aerosol

coagulation frequency predictions. *J. Colloid Interface Sci*. Nov 2002;255(1):10–26.
23. Schmid HJ, Al-Zaitone B, Artelt C, Peukert W. Evolution of the fractal dimension for simultaneous coagulation and sintering. *Chem Eng Sci*. 2006;61(1):293–305.
24. Zhou L, Rai A, Piekiel N, Ma XF, Zachariah MR. Ion-mobility spectrometry of nickel nanoparticle oxidation kinetics: application toe nergetic materials. *J Phys Chem C*. 2008;112(42):16209–16218.
25. Dikici B, Dean SW, Pantoya ML, Levitas VI, Jouet RJ. Influence of aluminum passivation on the reaction mechanism: flame propagation studies. *Energy & Fuels*. 2009;23:4231–4235.
26. Wang CM, Baer DR, Amonette JE, Engelhard MH, Antony J, Qiang Y. Morphology and electronic structure of the oxide shell on the surface of iron nanoparticles. *J Am Chem Soc*. 2009;131(25):8824–8832.
27. Rai A, Lee D, Park KH, Zachariah MR. Importance of phase change of aluminum in oxidation of aluminum nanoparticles. *J Phys Chem B*. 2004;108(39):14793–14795.
28. Sun J, Pantoya ML, Simon SL. Dependence of size and size distribution on reactivity of aluminum nanoparticles in reactions with oxygen and MoO3. *Thermochim Acta*. 2006;444(2):117–127.
29. Trunov MA, Schoenitz M, Zhu XY, Dreizin EL. Effect of polymorphic phase transformations in Al2O3 film on oxidation kinetics of aluminum powders. *Combust Flame*. 2005;140(4):310–318.
30. Aumann CE, Skofronick GL, Martin JA. Oxidation behavior of aluminum nanopowders. *J Vacuum Sci Technol B*. 1995;13(3):1178–1183.
31. Park K, Lee D, Rai A, Mukherjee D, Zachariah MR. Size-resolved kinetic measurements of aluminum nanoparticle oxidation with single particle mass spectrometry. *J Phys Chem B*. 2005;109(15):7290–7299.
32. Mukherjee D, Rai A, Zachariah MR. Quantitative laser-induced breakdown spectroscopy for aerosols via internal calibration: Application to the oxidative coating of aluminum nanoparticles. *J Aerosol Sci*. 2006;37(6):677–695.
33. Rai A, Park K, Zhou L, Zachariah MR. Understanding the mechanism of aluminium nanoparticle oxidation. *Combust Theory Model*. 2006;10(5):843–859.
34. Alavi S, Mintmire JW, Thompson DL. Molecular dynamics simulations of the oxidation of aluminum nanoparticles. *J Phys Chem B*. 2005;109(1):209–214.
35. Vashishta P, Kalia RK, Nakano A. Multimillion atom simulations of dynamics of oxidation of an aluminum nanoparticle and nanoindentation on ceramics. *J Phys Chem B*. 2006;110(8):3727–3733.
36. Zhang F, Gerrard K, Ripley RC. Reaction mechanism of aluminum-particle-air detonation. *J Propul Power*. 2009;25(4):845–858.
37. Trunov MA, Umbrajkar SM, Schoenitz M, Mang JT, Dreizin EL. Oxidation and melting of aluminum nanopowders. *J Phys Chem B*. 2006;110(26):13094–13099.
38. Xiong Y, Pratsinis SE. Formation of agglomerate particles by coagulation and sintering. 1. A 2-dimensional solution of the population balance equation. *J Aerosol Sci*. 1993;24(3):283–300.
39. Mandelbrot BB. *The Fractal Geometry of Nature*. New York: W. H. Freeman; 1983.
40. Meakin P, Witten TA. Growing interface in diffusion-limited aggregation. *Phys Rev A*. 1983;28(5):2985–2989.
41. Schmidtott A. New approaches to insitu characterization of ultrafine agglomerates. *J Aerosol Sci*. 1988;19(5):553–563.
42. Friedlander SK. *Smoke, Dust, and Haze*. New York: Oxford University Press; 2000.
43. Wu MK, Windeler RS, Steiner CKR, Bors T, Friedlander SK. Controlled synthesis of nanosized particles by aerosol processes. *Aerosol Sci Technol*. 1993;19(4):527–548.
44. Buffat P, Borel JP. Size effect on melting temperatures of gold particles. *Phys Rev A*. 1976;13(6):2287–2298.
45. Levenspiel O. *Chemical Reaction Engineering*. 2nd ed. New York, NY: John Wiley and Sons, Inc; 1962.
46. Kostoglou M, Konstandopoulos AG. Evolution of aggregate size and fractal dimension during Brownian coagulation. *J Aerosol Sci*. 2001;32(12):1399–1420.
47. German RM. *Sintering Theory and Practice*. New York, NY: John Wiley and Sons, Inc; 1996.
48. Assael MJ, Kakosimos K, Banish RM, et al. Reference data for the density and viscosity of liquid aluminum and liquid iron. *J Phys Chem Ref Data*. 2006;35(1):285–300.
49. Paradis P-F, Ishikawa T. Surface tension and viscosity measurements of liquid and undercooled alumina by containerless techniques. *Jap J Appl Phys*. 2005;44:5082–5085.
50. Sarou-Kanian V, Millot F, Rifflet JC. Surface tension and density of oxygen-free liquid aluminum at high temperature. *Int J Thermophys*. 2003;24(1):277–286.
51. Blackburn PE, Buchler A, Stauffer JL. Thermodynamics of vaporization in the aluminum oxide-boron oxide system. *J Phys Chem*. 1966;70(8):2469–2474.
52. Polyak EV, Sergeev SV. *Compt. Rend. (Doklady) Acad Sci. URSS*. 1941;33.
53. Samsonov G. *The Oxide Handbook*. New York: Springer; 1982.
54. Jensen JE, Tuttle WA, Stewart RB, Brechna H, Prodell AG. *Brookhaven national Laboratory Selected Cryogenic Data Notebook*. In: *Brookhaven National Laboratory Associated Universities, Inc. USDOE*, ed. Vol 1. Upton, NY: Brookhaven National Laboratory Associated Universities; 1980.
55. Munro RG. Evaluated material properties for a sintered alpha-alumina. *J Am Ceram Soc*. 1997;80(8):1919–1928.
56. Fuller EN, Schettler PD, Giddings JC. A new method for prediction of binary gas-phase diffusion coefficients. *Industrial & Eng. Chemistry* 1996;58(5):18–27.

Manuscript received Sept. 1, 2011, and revision received Nov. 18, 2011, and final revision received Jan. 10, 2012.